A New High-Order Spectral Difference Method for Simulating Viscous Flows on Unstructured Grids with Mixed-Element Meshes

by Mao Li

B.S. in Mechanical Engineering, July 2011, Zhejiang University

A Thesis submitted to

The Faculty of
The School of Engineering and Applied Science
of The George Washington University
in partial fulfillment of the requirements
for the degree of Master of Science

May 19, 2019

Thesis directed by

Chunlei Liang
Associate Professor of Mechanical and Aerospace Engineering

Charles A. Garris
Professor of Mechanical and Aerospace Engineering

© Copyright 2019 by Mao Li
All rights reserved

Acknowledgments

I am elated in thanking Dr. Chunlei Liang, my advisor. Dr. Liang was responsible, supportive, and made a great effort to keep a positive working atmosphere in the group. He has been considerate and patient, without his guidance the work would not have reached its goal. It has been a great pleasure to work with him and the student colleagues.

My sincere thanks to Dr. Charles A. Garris as my academic advisor after I was admitted to George Washington University. Dr. Garris was knowledgeable, kind, and always provided advice when I came to him.

I would also like to thank all the teaching and non-teaching staff of Department of Mechanical and Aerospace Engineering, for their support to us students.

Last but not the least, I would like to thank my parents, wife, friends.

This research has been supported by an Office of Naval Research (ONR) Young Investigator Program Award with award number N000141410367 (monitored by Dr. Ki-Han Kim) to Chunlei Liang.

Abstract

A New High-Order Spectral Difference Method for Simulating Viscous Flows on Unstructured Grids with Mixed-Element Meshes

In the present study, a spectral difference (SD) method is developed for viscous flows on meshes with a mixture of triangular and quadrilateral elements. The SD method was originally developed by Liu et al. [13] for simplex elements and has been studied for years. The standard SD method for triangular elements, which employs Lagrangian interpolating functions for fluxes, is not stable when the designed accuracy of spatial discretization is third order or higher. Unlike the standard SD method, the method examined here uses vector interpolating functions in the Raviart-Thomas (RT) spaces to construct continuous flux functions on reference elements. The spectral-difference Raviart-Thomas (SDRT) method was originally proposed by Balan et al. [1] and implemented on triangular-element meshes for invisid flow only. In the presented study, a rigorous linear stability analysis of spatial and full discretization was performed on two dimensional (2D) quadrilateral RT elements and mixed elements. We found that the current SDRT scheme is stable for fourth order accurate spatial discretizations while a stable fifth order SDRT scheme remains to be identified. A new 2D SDRT solver was developed for compressible Navier-Stokes equations that further extended the application of SDRT method to quadrilateral- and mixed-element meshes for both inviscid and viscous flows. Through different test cases and comparative numerical studies, our obtained results verified the stability and high-order accuracy of SDRT method by using triangular-, quadrilateral-, and mixed-element meshes for both inviscid and viscous flows.

Table of Contents

Acknowledgments . . . . . **iv**

Abstract . . . . . **v**

List of Figures . . . . . **vii**

List of Tables . . . . . **viii**

1 Introduction **1**

2 The spectral difference methods using Raviart-Thomas spaces (SDRT) . . . **5**

2.1 Element transformation, solution points, and flux points 5
2.2 Spectral difference method using Raviart-Thomas elements 8
2.3 Treatment of inviscid flux 10
2.4 Treatment of viscous flux 10
2.5 The final SDRT scheme 11

3 Linear stability analysis **13**

3.1 Analysis for spatial discretization 13
3.2 Analysis for Full Discretization 15

4 Results **19**

4.1 Accuracy Verification 19
4.1.1 2D linear-advection equation 19
4.1.2 2D isentropic vortex 21
4.1.3 2D viscous planar Couette flow 22
4.2 Inviscid flow past NACA0012 25
4.3 Viscous flow past a cylinder 26
4.3.1 Reynolds number 20 26
4.3.2 Reynolds number 100 29

5 Conclusions and Future Work **33**

Bibliography **34**

List of Figures

2.1 Mapping from physical domain (x,y) to computational domain (r,s). 5
2.2 Flux points (•) and solution points (⋄) arrangement for $SDRT_2$. 7

3.1 Mesh generation for linear stability analysis. 14
3.2 Fourier footprints of the second-, third- and fourth-order SDRT scheme on mixed-element meshes using upwind fluxes. 16

4.1 Hybrid-element meshes used. 20
4.2 Density (Rho) contours of a Euler vortex using the $SDRT_3$ scheme. 23
4.3 Density (Rho) contours of a moving Euler vortex using the $SDRT_3$ scheme. . 24
4.4 Mesh for moving Euler vortex. 24
4.5 Mesh for 2D viscous Coutte flow. 25
4.6 Mixed-element mesh of the NACA0012. 27
4.7 Pressure contour for NACA0012. 27
4.8 Pressure coefficient for NACA0012. 28
4.9 Mixed-element mesh of cylinder. 28
4.10 Drag coefficient against normalized physical time (UT/D) at Re =20 by $SDRT_2$. 29
4.11 Velocity streamlines around a cylinder at Re=20 by $SDRT_2$. 30
4.12 Vorticity contour around a cylinder at Re=100 by $SDRT_2$. 30
4.13 Lift coefficient against normalized physical time at Re = 100 by $SDRT_2$. . . 31
4.14 Drag coefficient against normalized physical time at Re = 100 by $SDRT_2$. . . 31

List of Tables

3.1 Mixed-element mesh maximum CFL number vs. Theta at skew angle= 90°. . 18

4.1 Accuracy of SDRT methods for the 2D wave equation. 20
4.2 Solution verification of $SDRT_3$ with quadrilateral elements for a Euler vortex. 22
4.3 Accuracy of SDRT methods for the 2D Euler vortex. 23
4.4 Accuracy of SDRT methods for 2D Couette flow. 26
4.5 SDRT results compared to benchmark solutions for flow over a cylinder at Re = 100. 32

Chapter 1: Introduction

High-order methods for computational fluid dynamics have been explored extensively by engineers and applied mathematicians over the past 30 years. In pursuit of a numerical method that is conservative, high order accurate, geometrically flexible, and computational efficient, this research focuses on the design of high-order spectral difference method for simplex elements. To achieve these properties, numbers of methods was developed and studied. To achieve efficiency and simplicity, structured grids are usually preferred. Finite difference (FD) method, which is the earliest method, has a one dimensional spatial differencing scheme along each coordinate direction. The FD method is also possible to be extended to be high-order accurate on structured grids. One example is the compact finite differencing method. While enjoying great efficiency and simplicity, the FD method is not a body-fitted-grid method and becomes not straightforward in dealing with complex geometries.

Finite volume (FV) methods were developed for the purpose to satisfy integral conservation law [7], in which unknowns are calculated in a cell average manner. The reconstruction of flux integral over cell boundaries is performed using neighbouring cell unknowns. Although geometric properties including cell volumes and surface vectors can be accurately calculated, the conventional FV method for unstructured grids is limited to second order accuracy because a high-order discretization stencil is non-trivial to construct for the FV method to deal with unstructured grids.

Aside from FD and FV method, the finite element (FE) method [6] is also becoming popular for solving fluid flow problems. The FE method can be used on unstructured grids and thus is geometrically flexible. In FE method, the computational domain is divided into small elements and unknowns are placed at similar geometrical points in each element. The local reconstruction of nodal values are universal for all elements with regard to the same

set of shape functions. Usually the Galerkin method is used to satisfy the conservation law in a weak form, and the law is satisfied for the global domain rather than for each element. FE methods can involve very large, sparse matrices in application.

FD, FV and FE methods mentioned above were usually for comparatively low order accurate simulations in practice. Those methods were proved to be reliable and stable so they are still widely used, while high order methods for unstructured grids, which can deal with challenging problems that requires high order accuracy in complex geometry, has become the field of interest. Only recently, studies of unsteady turbulent flows with complex geometries began to show that high-order methods can be several times faster and more accurate than commercial CFD softwares using the second-order FV methods, such as STAR-CCM+ [24] and ANSYS-FLUENT [8]. Discontinuous Galerkin (DG) method, first introduced by Reed and Hill [17] can be seen as one of the pioneers of such high order methods. The implementation of DG schemes usually require quadrature procedures and the original Runge-Kutta DG (RKDG) method developed by Cockburn et al. [4] suffers from drawbacks such as high computational cost with increasing order of accuracy. Improved methods such as nodal DG method were proposed to overcome those weaknesses.

To avoid the calculation of integrals and the procedures of quadrature, the spectral difference (SD) method was originally developed by Liu et al. [13, 26] for simplex elements and has been studied for the past decade. It combines the best features of finite-volume and finite-difference methods such as geometric flexibility and high computational efficiency. The SD method is widely viewed as an extension of the staggered-grid multidomain spectral method designed by Kopriva [9]. It shares some common features with DG method such as they both use discontinuous polynomial solution spaces, and use some Riemann solver to couple solutions between discontinuous elements at element interfaces. May [14] also pointed out the SD method is equivalent to the quadrature-free discontinuous Galerkin(DG) method at least in one dimension. Unfortunately, the SD method in its original form, as proposed by Liu et al, is proved by Abeele et al. [23] to have instability on triangular

elements. For triangles, Abeele analyzed and tested SD schemes of order of accuracy higher than two and tried to achieve stability by moving flux points while the effort was not successful. Balan et al. [1] adopted an alternative approach for flux interpolation using Raviart-Thomas spaces for triangular elements, which we refer to as the spectral-difference Raviart-Thomas (SDRT) method. The SDRT method overcomes the instability problem and at the same time reduces the number of degrees of freedom needed for high-order interpolation of a flux function over each element when compared to the standard SD method [1, 3, 28].

Moreover, the three dimensional (3D) SD method has been successfully developed on hexahedral meshes by Sun et al. [21] and was successfully used to simulate a turbulent channel flow by Liang et al. [12]. However, the SD method on simplex elements has not reached the same level of popularity for 3D simulations. In the research group of Professor Chunlei Liang, the high-order spectral difference method has been designed for simulations of stratified solar convection [25] and rotary wing aerodynamics [29]. However, the success in 3D simulations has been largely limited to hexahedral grids.

This MS thesis research aims to explore future practical applications of the spectral difference method on unstructured grids with simplex elements. Usually, quadrilateral elements are favored for solving boundary-layer problems, but mixed-element meshes with both quadrilateral and triangular elements are sometimes more straightforward in unstructured-grid generation. Studies have been done for the standard SD method on mixed-element meshes [11]. However, no test has been done on the SDRT method with quadrilateral elements. Its performance remains to be verified and validated.

For mixed-element meshes, we use two sets of shape functions for triangles and quadrilaterals, respectively, in order to setup the SDRT method. The SDRT scheme on triangular elements was studied and good performance was demonstrated [1, 3, 28]. In this study, we will extend the numerical experiments to include quadrilateral elements, and further test the performance of the SDRT method on mixed-element grids. In addition, studies on the

SDRT method were performed only for inviscid flows so far [1]. In this present study, we will extend the application of SDRT method to viscous flows.

The paper is organized as follows. Chapter 2 presents the SDRT numerical method in detail and Chapter 3 describes our linear stability analysis procedure. The work we have done and the results obtained is illustrated in Chapter 4. Chapter 5 concludes the work and proposes the plan for future work.

Chapter 2: The spectral difference methods using Raviart-Thomas spaces (SDRT)

2.1 Element transformation, solution points, and flux points

In describing the SDRT approach, we consider the unsteady compressible Navier-Stokes equations defined on a two-dimensional domain, represented here as

$$\frac{\partial Q}{\partial t} + \nabla_{xy} \cdot \boldsymbol{F} = 0, \tag{2.1}$$

where Q is the vector of conserved variables, $\boldsymbol{F} = \boldsymbol{F}_i(Q) - \boldsymbol{F}_v(Q, \nabla Q)$ is the total flux and where $\boldsymbol{F}_i$ and $\boldsymbol{F}_v$ are the inviscid and viscous flux vectors, respectively. We consider problems where the physical domain is discretized with, in general, a mixture of straight-sided triangular and quadrilateral elements. Triangular and quadrilateral elements in the physical domain (x, y) are transformed into either 1) equilateral-triangle reference elements or 2) square reference elements, respectively, in the computational domain (r, s). The transformation between the physical-element domain and the reference-element domain is shown in Figure 2.1.

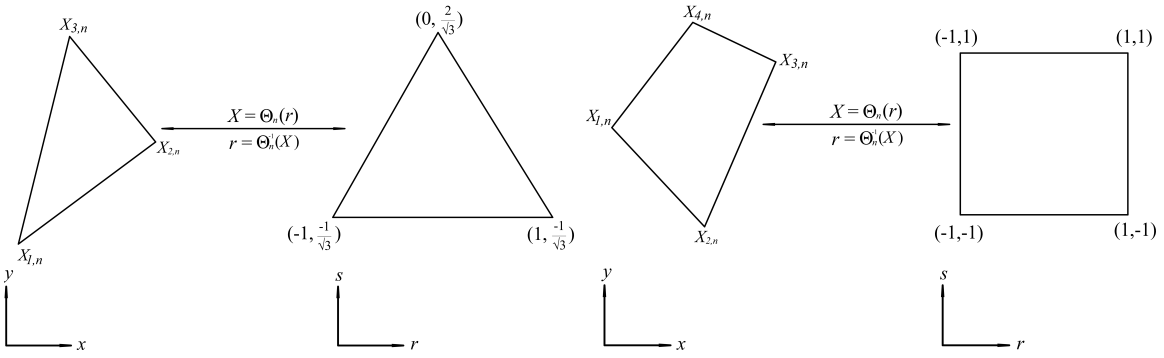

(a) Mapping for triangular elements.

(b) Mapping for quadrilateral elements.

Figure 2.1: Mapping from physical domain (x, y) to computational domain (r, s).

The mapping function for the equilateral-triangle element, n, is

$$\begin{aligned}\boldsymbol{X} = \Theta_n(r,s) = &\frac{(2-3r-\sqrt{3}s)}{6}\boldsymbol{X}_{1,n} + \frac{(2+3r-\sqrt{3}s)}{6}\boldsymbol{X}_{2,n} \\ &+\frac{(2+2\sqrt{3}s)}{6}\boldsymbol{X}_{3,n}\,,\end{aligned} \tag{2.2}$$

whereas the mapping function for the square element, n, is

$$\begin{aligned}\boldsymbol{X} = \Theta_n(r,s) = &\frac{(1-r)(1-s)}{4}\boldsymbol{X}_{1,n} + \frac{(1+r)(1-s)}{4}\boldsymbol{X}_{2,n} \\ &+\frac{(1+r)(1+s)}{4}\boldsymbol{X}_{3,n} + \frac{(1-r)(1+s)}{4}\boldsymbol{X}_{4,n}\,.\end{aligned} \tag{2.3}$$

The governing equation is then transformed into the computational domain as

$$\frac{\partial \widetilde{Q}}{\partial t} + \nabla_{rs}\cdot\widetilde{\boldsymbol{F}} = 0\,, \tag{2.4}$$

where

$$\widetilde{Q} = |\mathscr{J}|Q\,, \tag{2.5}$$

and

$$\widetilde{\boldsymbol{F}} = |\mathscr{J}|\mathscr{J}^{-1}\boldsymbol{F}\,, \tag{2.6}$$

The Jacobian matrix for the transformation is defined as

$$\mathscr{J} = \frac{\partial(x,y)}{\partial(r,s)} = \begin{bmatrix} x_r & x_s \\ y_r & y_s \end{bmatrix}. \tag{2.7}$$

Two sets of points are defined in the reference element: solution points and flux points. Unlike the standard SD method, the SDRT method does not assign flux points on element corner points. For triangular elements, the choice of edge flux point locations has no influence on stability [1]. Gauss-Legendre quadrature-point locations are used for flux points in the present study and the unit vectors defined at these points are outwards normal to

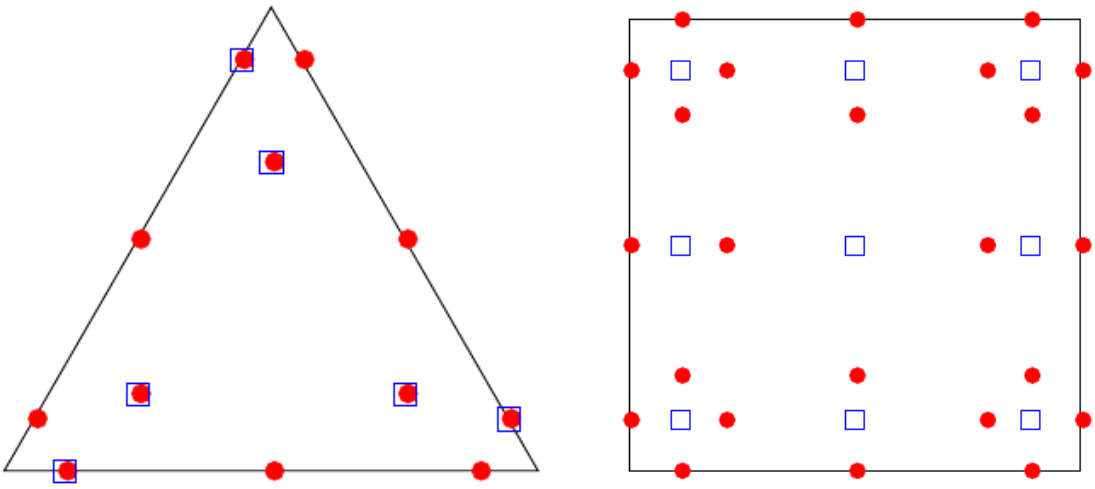

Figure 2.2: Flux points (•) and solution points (◇) arrangement for $SDRT_2$.

each element face. The locations of interior flux points have a notable influence on stability [1]. In the case of the first-order SDRT scheme, $SDRT_1$, the interior flux point is located on the centroid and two mutually orthogonal unit vectors collocate at this point, which forms two degrees of freedom. For the second-order $SDRT_2$ scheme, there are three interior flux points with two degrees of freedom on each point placed in the middle between the centroid and each vertex to maintain stability. For higher-order SDRT schemes, interior flux points are calculated by higher-order Gauss-Legendre quadrature rules. With respect to the SDRT method on quadrilateral elements, the arrangement of flux points is almost similar to the standard SD method. However, it is known that the choice of Chebyshev-Gauss-Lobatto points for computing nonlinear inviscid fluxes suffer from weak instability for quadrilateral elements [23]. Thus, we use Gauss-Legendre quadrature-points to locate the edge fluxes so it is possible to maintain stability and to pair the quadrilateral edge flux points with those of triangular elements. All interior flux points in quadrilateral elements have only one degree of freedom. The position of solution points has no influence on the linear stability of the SDRT scheme [1, 28]. An example of flux- and solution-point locations for $SDRT_2$ elements is presented in Figure 2.2.

2.2 Spectral difference method using Raviart-Thomas elements

The conserved variables on flux points are calculated from solution points as

$$\widetilde{Q}(r) = \sum_{i=1}^{N_m} \widetilde{Q}_i L_i(r)\,, \tag{2.8}$$

where $L_i(r), i = 1,2,3,\ldots,N_m$ are the shape functions and they are a basis of a polynomial space, P_m, with degree, m. N_m is the dimension of P_m, i.e., the number of functions needed to reconstruct these degree-m polynomials. In 2D, N_m is given by

$$N_m = \frac{(m+1)(m+2)}{2}\,, \tag{2.9}$$

for triangular elements, and

$$N_m = (m+1)^2\,, \tag{2.10}$$

for quadrilateral elements. For example, a typical polynomial ,P_m, for a triangular element with $m = 1$ is

$$P_1 = a + br + cs,$$

whereas a typical polynomial for a quadrilateral element with $m = 1$ is referred to as $P_{m,m}$, which has the form of

$$P_{1,1} = a + br + cs + drs\,.$$

RT_m is the smallest polynomial space such that its divergence maps RT_m onto P_m. We define the Raviart-Thomas (RT) space below spanned by the Raviart-Thomas basis functions of order, m, for the reference equilateral triangle and square, respectively:

$$RT_m(\Omega_s) = (P_m(\Omega_s))^2 + \begin{bmatrix} r & s \end{bmatrix}^T P_m(\Omega_s)\,, \tag{2.11}$$

for the reference triangle, Ω_s, and

$$RT_m(\Theta_s) = P_{m+1,m}(\Theta_s) \times P_{m,m+1}(\Theta_s)\,, \tag{2.12}$$

for the reference square, Θ_s, where

$$P_{k,l} = \sum_{i=0}^{k} \sum_{j=0}^{l} a_{ij} r^k s^l. \tag{2.13}$$

The two-dimensional RT_1 vector spaces spanned are

$$RT_1(\Omega_s) = \begin{bmatrix} a_1 + b_1 r + c_1 s + d_1 r^2 + d_2 rs \\ a_2 + b_2 r + c_2 s + d_1 rs + d_2 s^2 \end{bmatrix},$$

for the reference triangle, Ω_s, and

$$RT_1(\Theta_s) = \begin{bmatrix} a_1 + b_1 r + c_1 r^2 + d_1 s + e_1 rs + f_1 r^2 s \\ a_2 + b_2 s + c_2 s^2 + d_2 r + e_2 rs + f_2 rs^2 \end{bmatrix},$$

for the reference square, Θ_s. The dimensions of RT spaces are

$$N_m^{RT} = (m+1)(m+3)\,,$$

and

$$N_m^{RT} = 2(m+1)(m+2)\,,$$

for triangular and square elements, respectively.

In comparison with the standard SD method, the SDRT method reduces the total number of degrees of freedom by $2N_m - N_m^{RT}$ for interpolating the flux function of each triangular element.

In the standard SD method, fluxes are vectors and interpolation functions are scalars.

Conversely, in the SDRT method, interpolation functions, $\mathbf{\Psi}$, are vectors and fluxes are scalars. $\mathbf{\Psi}_j(r),\ j = 1,\ldots,N_m^{RT}$ form a basis in the Raviart-Thomas space, RT_m. These interpolation functions satisfy $\mathbf{\Psi}_j(r_k)\cdot \boldsymbol{s}_k = \delta_{jk}$, where r_k, $k = 1,\ldots,N_m^{RT}$ are flux points and $\boldsymbol{s}_k$ are unit vectors defined at these flux points. There are $m+1$ flux points on each edge of the reference element and the rest are located in the interior. On edge flux points, each numerical flux is used directly as the degree of freedom for the interpolation function. This is simpler than the standard SD method, in which the numerical flux is used as the normal component of the analytical flux and then degrees of freedom are obtained by projecting the numerical flux onto orthogonal directions.

2.3 Treatment of inviscid flux

Fluxes are not continuous across interfaces between elements. For the inviscid flux, a Riemann solver is applied to compute a common numerical flux. In this study, the Rusanov solver [18] is used and it has the following form

$$F_{inv} = \frac{1}{2}[(F_{inv,R} + F_{inv,L})\cdot \boldsymbol{n} - \lambda_{max}(Q_R - Q_L)]\,. \tag{2.14}$$

Here $\lambda_{max} = |V_n| + c$ is the absolute value of maximum characteristic speeds, V_n is the velocity magnitude normal to the edge, and c is the sound speed.

As for interior flux points, the degrees of freedom for flux-function interpolation are calculated by $F_j = |\mathscr{J}|\,\mathscr{J}^{-1}\boldsymbol{F}_j\cdot \boldsymbol{s}_k$.

2.4 Treatment of viscous flux

To get the numerical viscous flux, $\boldsymbol{F}_v(Q,\nabla Q)$, the following steps are used. The procedure is similar to the Bassi-Rebay I scheme [2].

- Use Equation (2.8) to get Q_f at flux points from the solution points. The subscripts, f, stands for flux points.

- Average Q_f on the element interfaces and apply boundary conditions for u,v,T.

- ∇Q at solution points are calculated by

$$\nabla Q_{s,i} = \sum_{j=1}^{N_m^{RT}} Q_{f,j} \boldsymbol{n}_j (\nabla_{rs} \cdot \boldsymbol{\Psi}_j(r_i)), \tag{2.15}$$

  where the subscripts, s, stands for solution points, $\boldsymbol{n}_j$ are unit vectors defined at flux points; $i = 1,\ldots,N_m$ is the index of solution points and $j = 1,\ldots,N_m^{RT}$ is index of degrees of freedom for flux-function interpolation.

- Reconstruct ∇Q_f at flux points using Equation (2.8), then average them on the element interfaces.

- Use the averaged Q_f and ∇Q_f to get the viscous-flux vectors.

2.5 The final SDRT scheme

The flux function on solution points is approximated in the RT space as

$$\widetilde{\boldsymbol{F}}(r_i) = \sum_{i=1}^{N_m^{RT}} F_j \boldsymbol{\Psi}_j(r_i), \tag{2.16}$$

where F_j is the total numerical flux consisting of both the inviscid and viscous flux. The divergence of flux function at solution points is calculated by

$$\nabla_{rs} \cdot \widetilde{\boldsymbol{F}}(r_i) = \sum_{j=1}^{N_m^{RT}} F_j (\nabla_{rs} \cdot \boldsymbol{\Psi}_j(r_i)). \tag{2.17}$$

In each cell, k, the time derivative of conserved variables at solution points, i, are

$$\frac{\partial \widetilde{Q}_i^k}{\partial t} = -\frac{1}{|\mathscr{J}^k|} \sum_{j=1}^{N_m^{RT}} F_j (\nabla_{rs} \cdot \boldsymbol{\Psi}_j(r_i)). \tag{2.18}$$

In the above two equations, $i = 1, \ldots, N_m$ is the index of solution points and $j = 1, \ldots, N_m^{RT}$ is the index of degrees of freedom for flux-function interpolation. Throughout this paper, time marching is performed using a fourth-order five-stage strong stability-preserving (SSP) Runge-Kutta scheme [20] to minimize the influence of temporal error.

Chapter 3: Linear stability analysis

In the present study, we follow the approach described in Van den Abeele et al. [23] and extend the linear stability analysis to quadrilateral RT elements and mixed elements. Linear stability analysis of spatial and full discretization on 1D elements and 2D triangular RT elements was performed in [1, 28, 15], which is not repeated here.

As to the analysis on 2D quadrilateral RT elements and mixed elements, we consider the 2D advection equation.

$$\frac{\partial u}{\partial t} + \nabla \cdot (\boldsymbol{a} u) = 0\,, \tag{3.1}$$

where $\boldsymbol{a} = ||\boldsymbol{a}||[\cos\psi \ \sin\psi]^T$ is the propagation velocity.

3.1 Analysis for spatial discretization

Substitute the following Fourier mode plane harmonic wave into Equation (3.1).

$$u(x,y,t) = \tilde{u} e^{(I\boldsymbol{k}\cdot\boldsymbol{r} - I\omega t)}\,, \tag{3.2}$$

where $I = \sqrt{-1}$, $\boldsymbol{r} = [x \ y]^T$, and $\boldsymbol{k} = k[\cos\theta \ \sin\theta]^T$. We can get the exact dispersion relation

$$\omega = ||\boldsymbol{a}|| k \cos(\psi - \theta)\,, \tag{3.3}$$

where ω is the frequency and k is the wave number.

The process of mesh generation is showed in Figure 3.1. Two vectors, $\boldsymbol{B}_1$ and $\boldsymbol{B}_2$, define the mesh-generating pattern. Using ΔB, the length of $\boldsymbol{B}_1$, these vectors are nondimensionalized as $\boldsymbol{B}_1' = \boldsymbol{B}_1/\Delta B$ and $\boldsymbol{B}_2' = \boldsymbol{B}_2/\Delta B$. In this case, a straightforward setting, $\boldsymbol{B}_1' = [1\ 0]^T$ and $\boldsymbol{B}_2' = [0\ 1]^T$ is applied. For mixed elements, the element to be analyzed is further divided into smaller subelements.

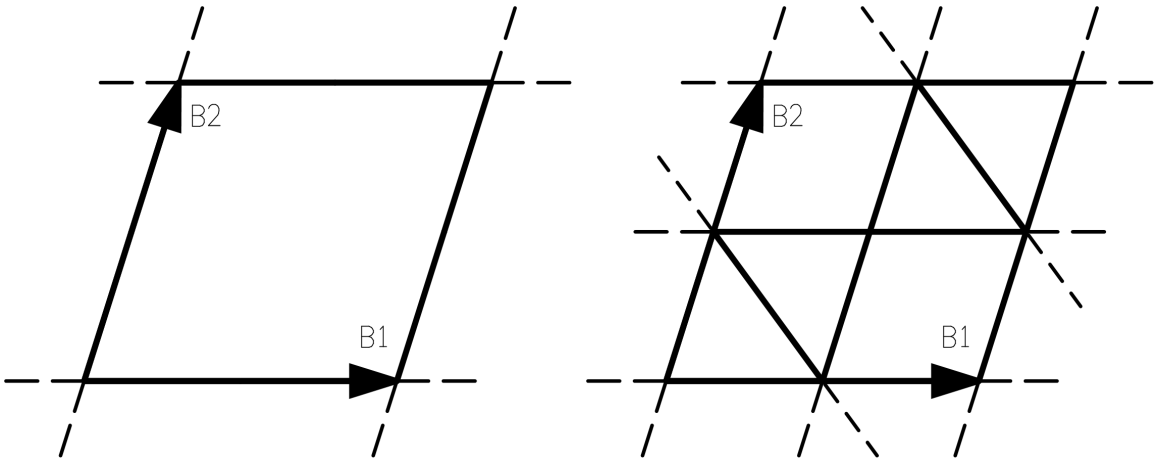

(a) Quadrilateral-element mesh (b) Mixed-element mesh.

Figure 3.1: Mesh generation for linear stability analysis.

In this case, upwind flux is used on element edges. Equation (3.1) is discretized in space into the following form:

$$\begin{aligned}\frac{\partial \tilde{u}_{i,j}}{\partial t} + \frac{||\boldsymbol{a}||}{\Delta B} D(M^{-1,0}u_{i-1,j} + M^{0,-1}u_{i,j-1} + M^{0,0}u_{i,j} \\ + M^{+1,0}u_{i+1,j} + M^{0,+1}u_{i,j+1}) = 0\,,\end{aligned} \tag{3.4}$$

where i and j are index numbers. M matrices are interpolating functions that extrapolate solutions to flux points, whereas the D matrix is used to compute the derivatives of flux at solution points. As to mixed RT elements, M and D matrices are calculated by assembling the matrices of subelements. The expression of a plane Fourier wave become

$$u_{i,j}(t) = \tilde{u}e^{[I\boldsymbol{k}\cdot(i\boldsymbol{B}_1 + j\boldsymbol{B}_2) - I\tilde{\omega}t]}\,, \tag{3.5}$$

and it is substituted into Equation (3.4). With non-dimensionalized wave number and frequency, $\boldsymbol{K} = \boldsymbol{k}\Delta B = K[\cos\theta \;\; \sin\theta]^T$, $\widetilde{\Omega} = \tilde{\omega}\Delta B/||\boldsymbol{a}||$, we can obtain the following

homogeneous linear equation system:

$$\begin{aligned}[-I\widetilde{\Omega}E + D(M^{-1,0}e^{-I\boldsymbol{K}\cdot\boldsymbol{B}'_1} + M^{0,-1}e^{-I\boldsymbol{K}\cdot\boldsymbol{B}'_2} + M^{0,0} \\ + M^{+1,0}e^{+I\boldsymbol{K}\cdot\boldsymbol{B}'_1} + M^{0,+1}e^{+I\boldsymbol{K}\cdot\boldsymbol{B}'_2})]\tilde{u} = 0\,.\end{aligned} \tag{3.6}$$

This equation is true for solutions of $\tilde{u}$ different from zero only when

$$\begin{aligned}\det[-I\widetilde{\Omega}E + D(M^{-1,0}e^{-I\boldsymbol{K}\cdot\boldsymbol{B}'_1} + M^{0,-1}e^{-I\boldsymbol{K}\cdot\boldsymbol{B}'_2} + M^{0,0} \\ + M^{+1,0}e^{+I\boldsymbol{K}\cdot\boldsymbol{B}'_1} + M^{0,+1}e^{+I\boldsymbol{K}\cdot\boldsymbol{B}'_2})] = 0\,,\end{aligned} \tag{3.7}$$

Let

$$\begin{aligned}Z = -D(M^{-1,0}e^{-I\boldsymbol{K}\cdot\boldsymbol{B}'_1} + M^{0,-1}e^{-I\boldsymbol{K}\cdot\boldsymbol{B}'_2} + M^{0,0} \\ + M^{+1,0}e^{+I\boldsymbol{K}\cdot\boldsymbol{B}'_1} + M^{0,+1}e^{+I\boldsymbol{K}\cdot\boldsymbol{B}'_2})\,,\end{aligned} \tag{3.8}$$

where Z is the Fourier footprint of the spatial discretization. $Z = Re + Im$, the real part Re, measures the diffusive properties while the imaginary part Im, measures the dispersive properties. For a stable numerical scheme, Re should always be non-positive.

Figure 3.2 shows the Fourier footprints of the SDRT schemes. The results indicate stability of all three schemes for mixed elements. Different combinations of elements were tested in addition to Figure 3.1b and the same conclusion can be drawn. Attempts to extend the SDRT scheme to a higher order was made. However, using the flux point locations suggested by Williams et al. [27], the SDRT_4 scheme suffers from a weak-instability problem with triangular elements.

3.2 Analysis for Full Discretization

Linear stability for the full discretization (space and time) is performed and the fourth-order SSP Runge-Kutta scheme is used for time discretization. Solution u^{n+1} is obtained from u^n

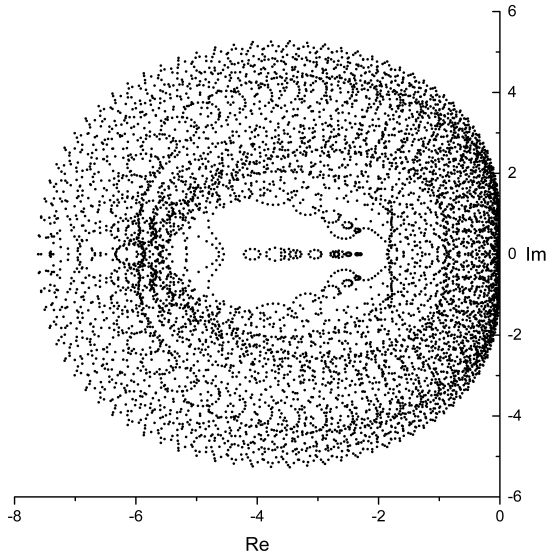

(a) RT1.

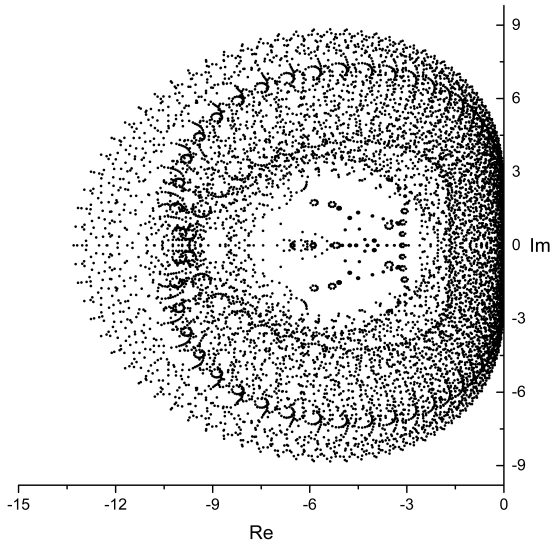

(b) RT2.

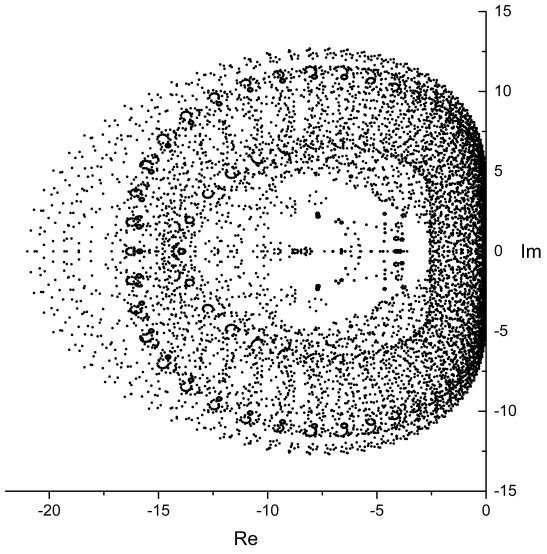

(c) RT3.

Figure 3.2: Fourier footprints of the second-, third- and fourth-order SDRT scheme on mixed-element meshes using upwind fluxes.

as Equation 3.9.

$$
\begin{aligned}
w^{(0)} =& u^n \\
w^{(k)} =& \sum_{l=0}^{k-1} \alpha_{kl} w^{(l)} + \nu \beta_{kl} Z w^{(l)}, k = 1, 2, \ldots, p \\
u^{n+1} =& w^{(p)}.
\end{aligned}
\tag{3.9}
$$

In the above equation, ν is the Courant-Friedrichs-Lewy(CFL) number. For the SSP scheme used in the present study, $p = 5$ is the stage number, and α and β are given by

$$
\alpha = \begin{bmatrix}
1 & & & & \\
0.444370494067 & 0.555629505932 & & & \\
0.620101851385 & 0 & 0.379898148615 & & \\
0.178079954108 & 0 & 0 & 0.821920045892 & \\
0.006833258840 & 0 & 0.517231672090 & 0.127598311333 & 0.348336757737
\end{bmatrix}, \tag{3.10}
$$

$$
\beta = \begin{bmatrix}
0.391752227004 & & & & \\
0 & 0.368410592630 & & & \\
0 & 0 & 0.251891774247 & & \\
0 & 0 & 0 & 0.544974750212 & \\
0 & 0 & 0 & 0.084604163382 & 0.226007483194
\end{bmatrix}. \tag{3.11}
$$

An alternative expression to get u^{n+1} is

$$
u^{n+1} = G u^n. \tag{3.12}
$$

Here G is the amplification factor, which has the following form at each stage

$$
\begin{aligned}
G^{(0)} =& I \\
G^{(k)} =& \sum_{l=0}^{k-1} (\alpha_{kl} I + \nu \beta_{kl} Z) G^{(l)}, k = 1, 2, \ldots, p.
\end{aligned}
\tag{3.13}
$$

Table 3.1: Mixed-element mesh maximum CFL number vs. Theta at skew angle= 90°.

	$\theta = 0$	$\theta = \pi/8$	$\theta = \pi/4$
$SDRT_1$	0.667	0.528	0.490
$SDRT_2$	0.391	0.325	0.299
$SDRT_3$	0.257	0.224	0.206

For the SSP scheme, $G^{(5)}$ is the amplification matrix and its spectral radius should always be smaller than one for any skew angle and advection angle. The SSP scheme is stable at a CFL condition and the maximum stable CFL number at a specific skew angle with a few advection angels is presented in Table 3.1.

Chapter 4: Results

The performance of the SDRT method with triangular elements is validated [1, 3, 28], yet it has not been tested on quadrilateral elements. Therefore, a SDRT solver that can use all triangular-, quadrilateral-, and hybrid-element meshes is developed. The accuracy of the SDRT method with quadrilateral element is first verified, some of the results are revealed in Section 4.1.2. Several attempts were made to achieve an order of accuracy higher than 4 but no ideal results were gained. The arrangement of flux points for a higher-order requires further studies.

4.1 Accuracy Verification

4.1.1 2D linear-advection equation

The 2D advection equation is tested using the following governing equation

$$\frac{\partial u}{\partial t} + \frac{\partial u}{\partial x} + \frac{\partial u}{\partial y} = 0\,. \tag{4.1}$$

The computational domain is $[-1,1] \times [-1,1]$. The initial condition $u_0 = sin(\pi(x+y))$ and periodic boundary conditions are applied. The total simulation time is $t = 2.0$. To better verify the performance of the SDRT method on hybrid-element meshes, tests were conducted on two different sets of meshes. The first set has a single layer of quadrilateral elements on boundaries, whereas the interior is filled with triangular elements. The other set has $2 \times 2 \times 2$ triangular elements in the center, whereas the rest are quadrilateral elements. Samples of meshes are presented in Figure 4.1.

The order of accuracy obtained for the SDRT$_m$ scheme is approximately $m+1$. The results are presented in Table 4.1.

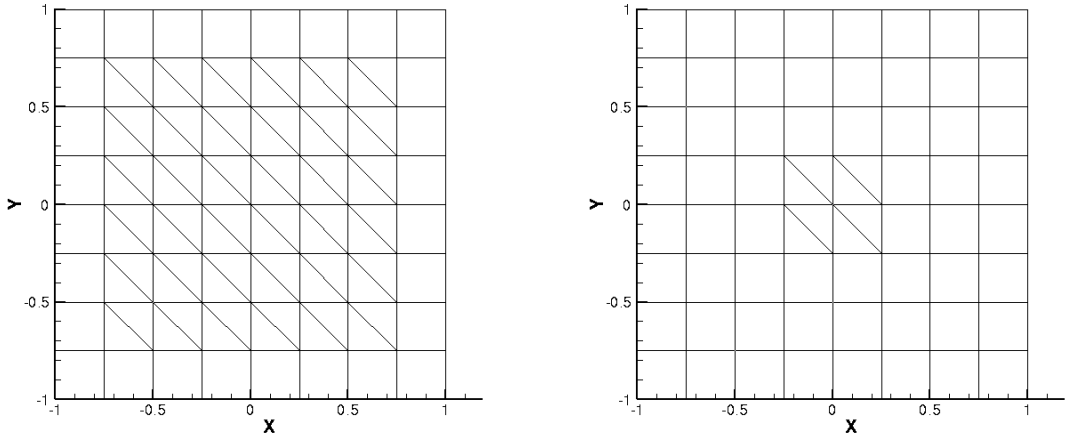

(a) Hybrid-element mesh set 1 -HB1.

(b) Hybrid-element mesh set 2 -HB2.

Figure 4.1: Hybrid-element meshes used.

Table 4.1: Accuracy of SDRT methods for the 2D wave equation.

Mesh set*	Degree	Time step	Tri/Quad cell	L2 error	Order
HB1	P1	1e-2	72/28	1.43e-1	-
		1e-2	392/60	3.31e-2	2.00
		1e-3	1800/124	7.18e-3	2.07
	P2	1e-2	72/28	3.21e-3	-
		1e-2	392/60	3.63e-4	3.13
		1e-3	1800/124	4.57e-5	2.96
	P3	1e-2	72/28	1.08e-4	-
		1e-2	392/60	5.92e-6	4.14
		1e-3	1800/124	6.50e-7	4.06
HB2	P1	1e-2	8/60	1.92e-1	-
		1e-2	8/252	5.54e-2	1.80
		1e-3	8/1020	1.43e-2	1.96
	P2	1e-2	8/60	4.99e-3	-
		1e-2	8/252	6.40e-4	2.98
		1e-3	8/1020	8.45e-5	2.94
	P3	1e-2	8/60	1.79e-4	-
		1e-2	8/252	1.09e-5	4.03
		1e-3	8/1020	6.50e-7	4.13

* Mesh set numbers correspond to Figure 4.1.

4.1.2 2D isentropic vortex

For this problem, the governing equations are the 2D Euler equations in conservative form

$$\frac{\partial u}{\partial t}+\frac{\partial f(u)}{\partial x}+\frac{\partial g(u)}{\partial y}=0\,, \tag{4.2}$$

where u, f, and g are

$$u=\begin{bmatrix}\rho\\ \rho u\\ \rho v\\ E\end{bmatrix}\quad f=\begin{bmatrix}\rho u\\ \rho u^2\\ \rho uv\\ u(E+p)\end{bmatrix}\quad g=\begin{bmatrix}\rho v\\ \rho uv\\ \rho v^2\\ v(E+p)\end{bmatrix}.$$

Here, ρ is the density of the fluid, u and v are velocity components in the x and y direction, respectively, p is the pressure, and E is the total energy. In this case, we apply the ideal gas law to get the relation between p and E as

$$p=(\gamma-1)(E-\frac{1}{2}\rho(u^2+v^2))\,. \tag{4.3}$$

We take $\gamma=1.4$, which is the specific heat capacity ratio for air. The mean flow values are ρ,p,u,v=1,1,0,0 and the vortex is added to the mean flow via perturbations in u, v, temperature, $T\propto\frac{p}{\rho}$, and entropy, $S\propto\frac{p}{\rho^\gamma}$:

$$\begin{aligned}\delta u&=-y\frac{\varepsilon}{2\pi}e^{0.5(1-r^2)}\,,\\ \delta v&=x\frac{\varepsilon}{2\pi}e^{0.5(1-r^2)}\,,\\ \delta T&=-\frac{(\gamma-1)\varepsilon^2}{8y\pi^2}e^{(1-r^2)}\,,\\ \delta S&=0\,,\end{aligned} \tag{4.4}$$

where ε is the vortex strength and $r^2=x^2+y^2$. The vortex remains at the same place since there is no mean flow. SDRT_1, SDRT_2, and SDRT_3 methods are applied to the problem.

Table 4.2: Solution verification of $SDRT_3$ with quadrilateral elements for a Euler vortex.

Mesh set	Degree	Time step	Mesh size	L2 error	Order
QUAD	P3	1e-2	8×8	1.23e-5	-
		1e-2	16×16	8.37e-7	3.88
		1e-3	32×32	5.28e-8	3.99

Regarding time marching, the same SSP five-stage Runge-Kutta method is applied. The L_2 error and order of accuracy of $SDRT_3$ method with quadrilateral elements is presented in Table 4.2.

Table 4.3 presents the L_2 error and orders of accuracy for SDRT methods using mixed-element meshes. Figure 4.2 is a plot of the density at $t = 0.2$ using the mesh presented in Figure 4.1a and the $SDRT_3$ scheme.

An alternative condition with mean flow values $u, v = 1, 1$ is tested in the computational domain $[-5,5] \times [-5,5]$. The left and right domains comprise quadrilateral and triangular elements, respectively. The vortex center is initially set at $[-1,-1]$. Figure 4.3 is the plot of the vortex crossing the center line and Figure 4.4 is the mesh used.

4.1.3 2D viscous planar Couette flow

A compressible planar Couette flow with an analytical solution is used to verify the accuracy of the viscous solver. The computational domain is [0,2]×[0,1]. One exemplar mesh is shown in Figure 4.5. At $y = 1$, a moving wall no-slip boundary with constant temperature and specified external pressure is applied. At $y = 0$, a stationary wall no-slip boundary with constant temperature is used. In the stream-wise direction, a periodic boundary condition is applied.

Table 4.3: Accuracy of SDRT methods for the 2D Euler vortex.

Mesh set*	Degree	Time step	Tri/Quad cell	L2 error	Order
HB1	P1	1e-2	72/28	5.12e-3	-
		1e-2	392/60	1.40e-3	1.78
		1e-3	1800/124	3.65e-4	1.88
	P2	1e-2	72/28	5.14e-4	-
		1e-2	392/60	8.37e-5	2.51
		1e-3	1800/124	1.24e-5	2.70
	P3	1e-2	72/28	1.60e-5	-
		1e-2	392/60	1.20e-6	3.62
		1e-3	1800/124	7.11e-8	4.00
HB2	P1	1e-2	8/60	4.17e-3	-
		1e-2	8/252	9.74e-4	2.13
		1e-3	8/1020	2.40e-4	2.02
	P2	1e-2	8/60	2.39e-4	-
		1e-2	8/152	3.52e-5	2.80
		1e-3	8/1020	5.08e-6	2.80
	P3	1e-2	8/60	1.08e-5	-
		1e-2	8/152	7.11e-7	3.96
		1e-3	8/1020	4.75e-8	3.91

* Mesh set numbers correspond to Figure 4.1.

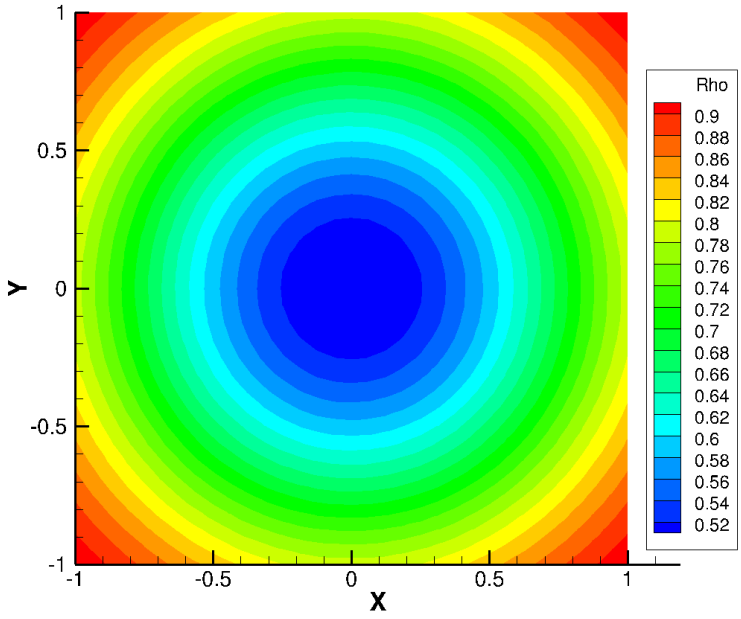

Figure 4.2: Density (Rho) contours of a Euler vortex using the $SDRT_3$ scheme.

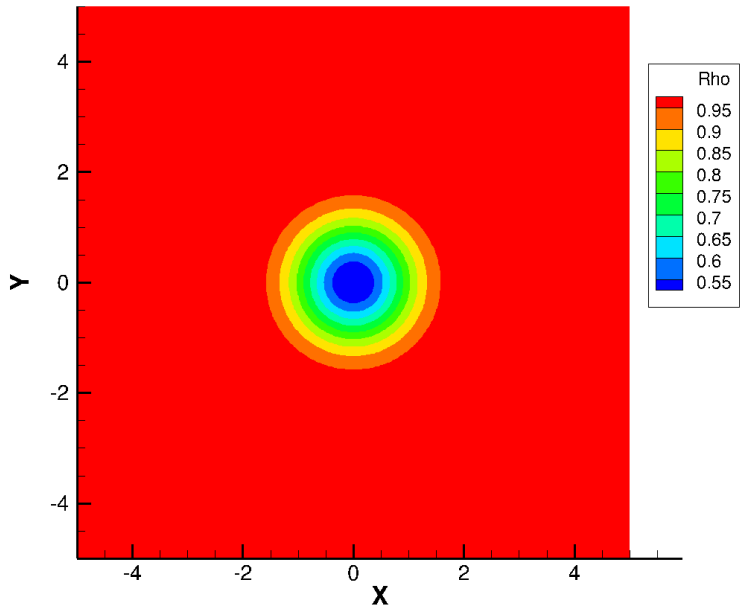

Figure 4.3: Density (Rho) contours of a moving Euler vortex using the $SDRT_3$ scheme.

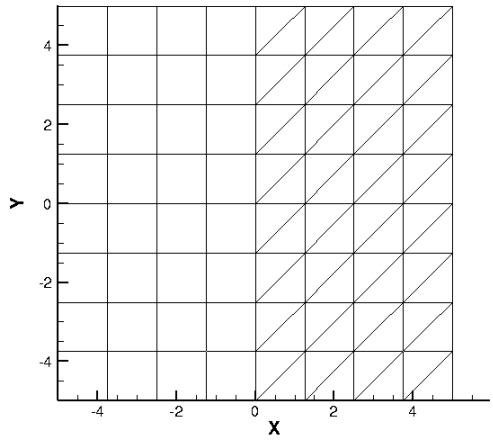

Figure 4.4: Mesh for moving Euler vortex.

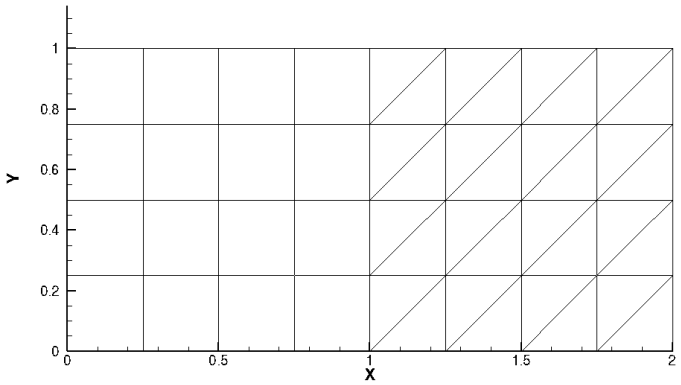

Figure 4.5: Mesh for 2D viscous Coutte flow.

The analytical solution is

$$\begin{aligned} u &= \frac{y}{H}U\,, \\ v &= 0\,, \\ e &= e_b + \frac{y}{H}(e_t - e_b) + \frac{PrU^2}{2\gamma}(\frac{y}{H} - (\frac{y}{H})^2)\,, \\ p &= constant\,, \end{aligned} \tag{4.5}$$

where $e = C_v T$ is the internal energy, subscripts t and b refer to top and bottom surfaces, and Pr is the Prandtl number, which is 0.72 in this case. As shown in Table 4.4, the designed accuracy in space is achieved for the second-, third-, and fourth-order respectively even on mixed element meshes.

4.2 Inviscid flow past NACA0012

The exact NACA0012 formula defining the geometry is

$$y = \pm 0.6 \times (0.29690x^{0.5} - 0.12600x - 0.35160x^2 + 0.28430x^3 - 0.10150x^4).$$

Table 4.4: Accuracy of SDRT methods for 2D Couette flow.

Degree	Time step	Tri/Quad cell	L2 error	Order
P1	1e-4	8/4	2.92e-4	-
	1e-4	32	16 7.29e-5	2.00
	1e-4	128	64 1.86e-5	1.97
P2	1e-4	8/4	1.55e-6	-
	1e-4	32/16	1.91e-7	3.02
	1e-4	128/64	2.34e-8	3.02
P3	1e-4	8/4	1.06e-8	-
	1e-4	32/16	7.94e-10	3.74
	1e-4	128/64	4.38e-11	4.18

The mixed-element mesh is shown in Figure 4.6. The Mach number is set to 0.63 and the angle of attack is 2° [5]. The $SDRT_3$ scheme is used. High order elements were used on the airfoil surface. The maximum Mach number obtained is less than 1. The pressure-contour result is presented in 4.7 and a plot of the surface pressure coefficient is shown in Figure 4.8a. Compared to the plot in Figure 4.8b and results from references, we can say that our solver is accurate.

4.3 Viscous flow past a cylinder

Viscous flow past a cylinder is investigated with Reynolds numbers of 20 and 100. A mixed-element mesh with quadrilateral and triangular elements is used. A nonreflecting boundary condition is applied on top and bottom boundaries. Figure 4.9 shows the area near the cylinder and the mesh used. High-order elements were used on the surface of the cylinder.

4.3.1 Reynolds number 20

The convergence rate for $SDRT_2$ is presented in Figure 4.10. The predicted drag coefficient is 2.089. Compared to the value 2.1 measured by Tritton [22] and 2.08 computed by Liang [10]. Velocity streamlines around a cylinder at a Reynolds number of 20 simulated by

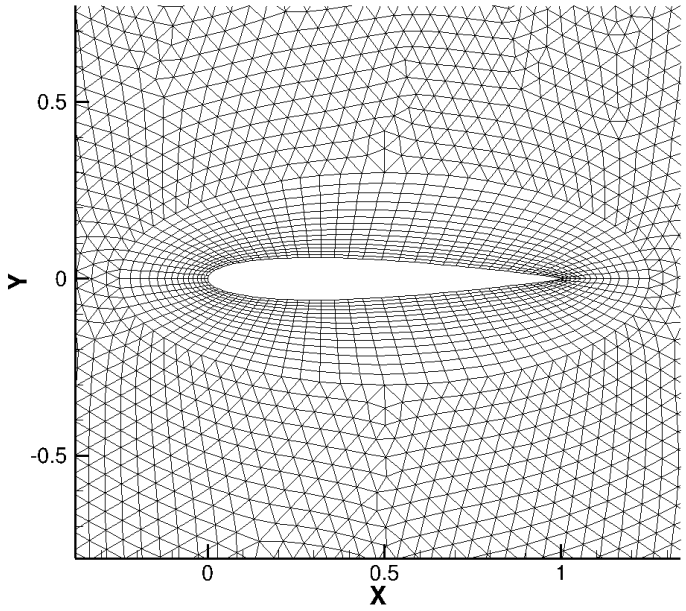

Figure 4.6: Mixed-element mesh of the NACA0012.

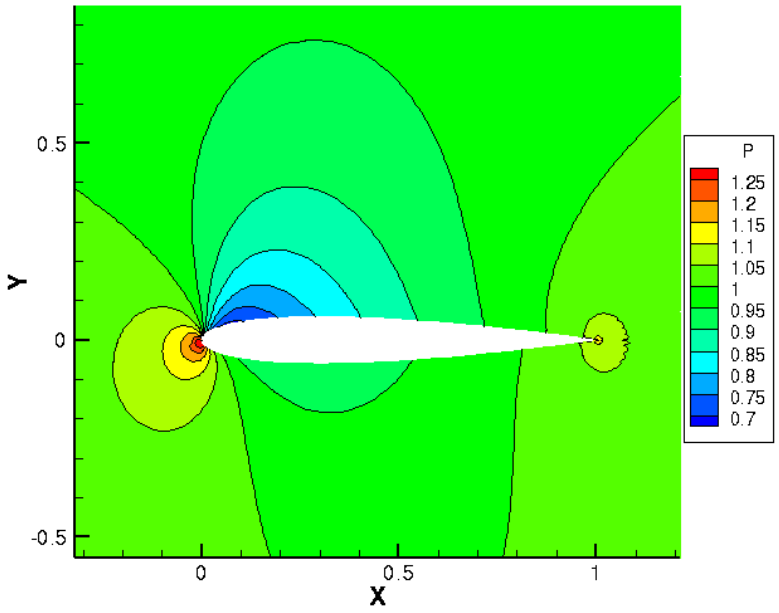

Figure 4.7: Pressure contour for NACA0012.

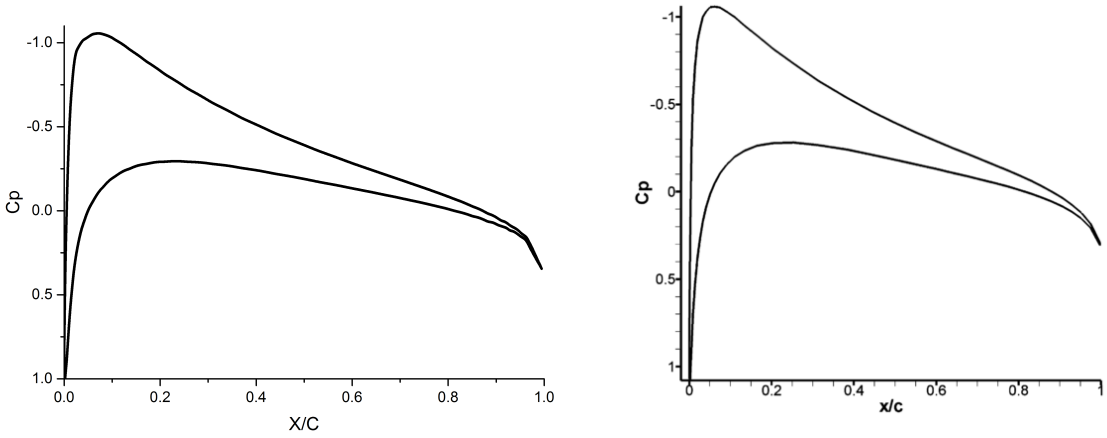

(a) Result from presented study

(b) Result from [11]

Figure 4.8: Pressure coefficient for NACA0012.

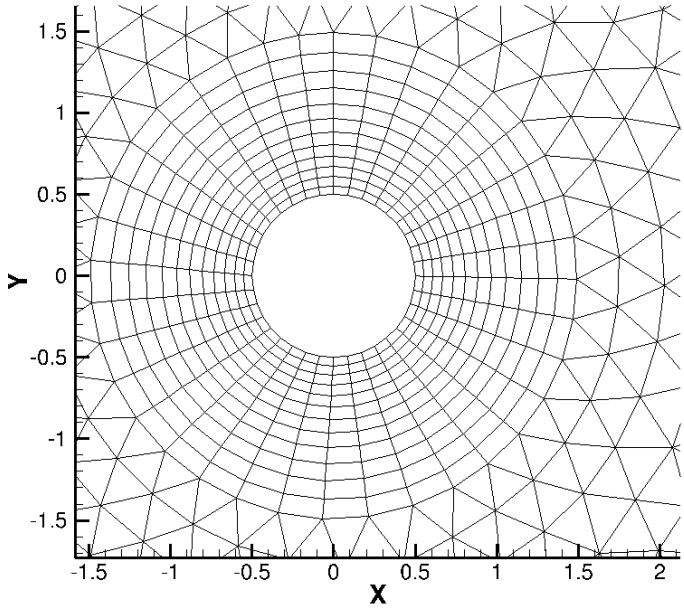

Figure 4.9: Mixed-element mesh of cylinder.

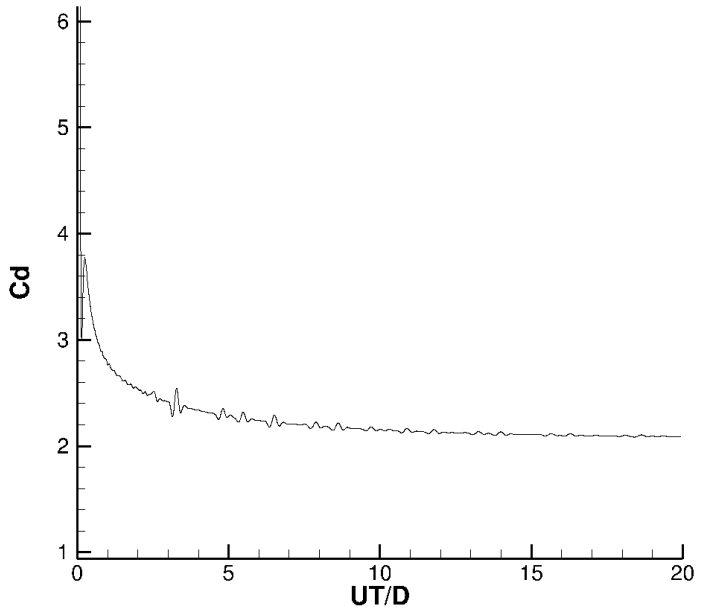

Figure 4.10: Drag coefficient against normalized physical time (UT/D) at Re =20 by $SDRT_2$.

$SDRT_2$ is presented in Figure 4.11.

4.3.2 Reynolds number 100

Flow past a cylinder at a Reynolds number of 100 is investigated by $SDRT_2$ as well. Figure 4.12 shows the vorticity behind the cylinder. Lift and drag coefficients against normalized physical time are presented in Figure 4.13 and Figure 4.14, respectively. Root-mean-square(RMS) values are used to present the fluctuating lift component, $Cl_{RMS} = \sqrt{\sum_{i=1}^{N}(Cl_i - Cl_{mean})^2/N}$. Cl_{RMS}, later referred to as Cl' is the RMS value of the lift coefficient. Cl_i is the lift coefficient at a single time point and Cl_{mean} is the mean value of N sample points. All these numbers are found in a single vortex shedding cycle. Table 4.5 shows the RMS lift coefficient and the Strohal number obtained from current work and previous studies.

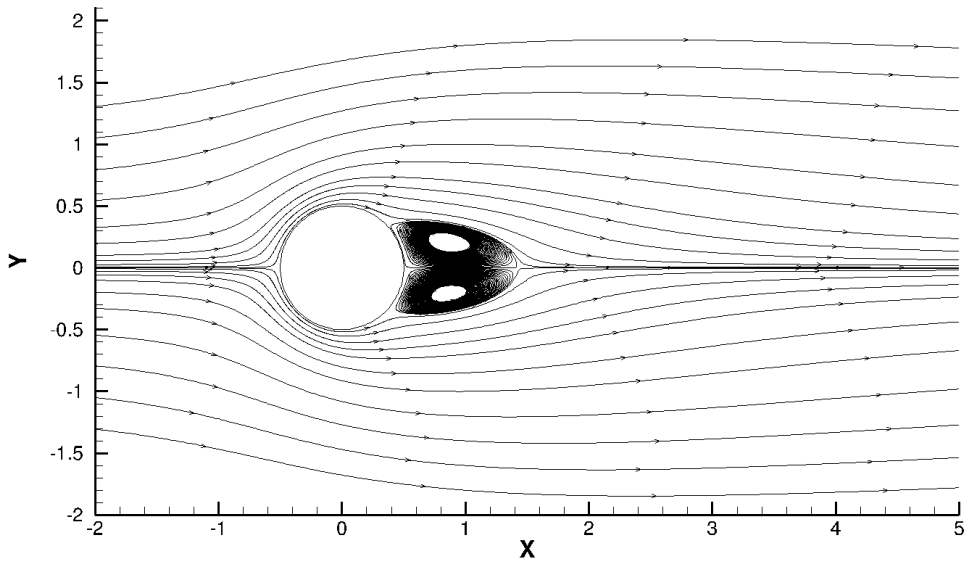

Figure 4.11: Velocity streamlines around a cylinder at Re=20 by SDRT$_2$.

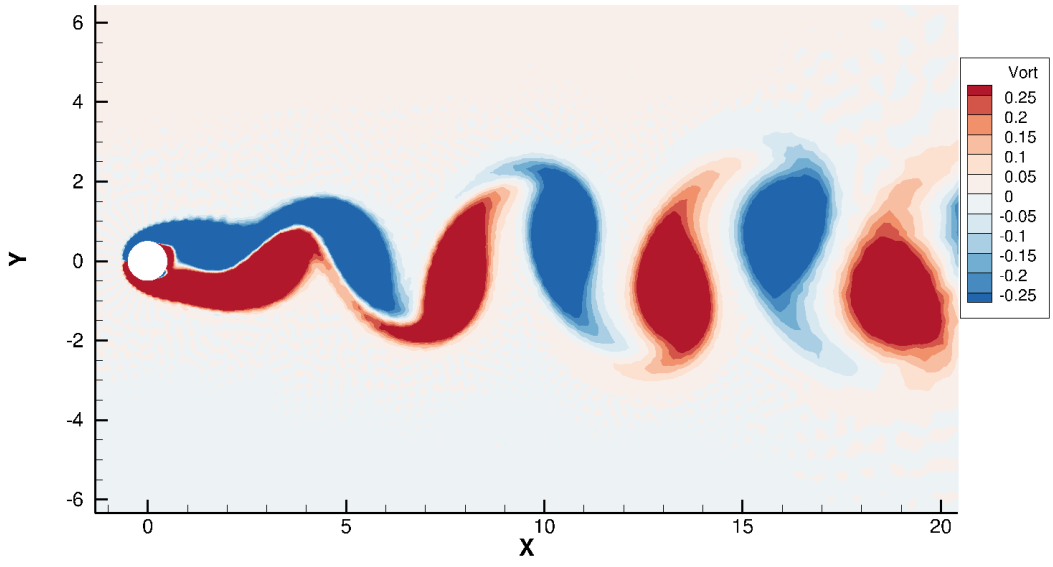

Figure 4.12: Vorticity contour around a cylinder at Re=100 by SDRT$_2$.

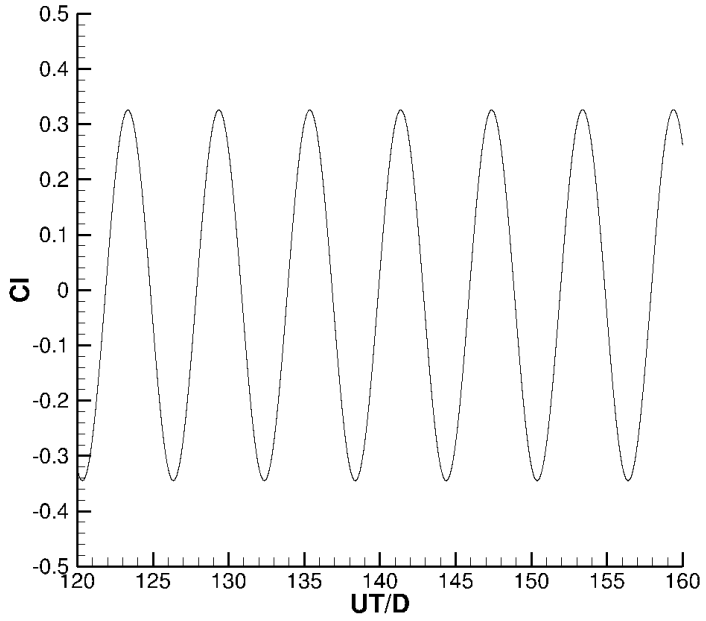

Figure 4.13: Lift coefficient against normalized physical time at Re = 100 by SDRT $_2$.

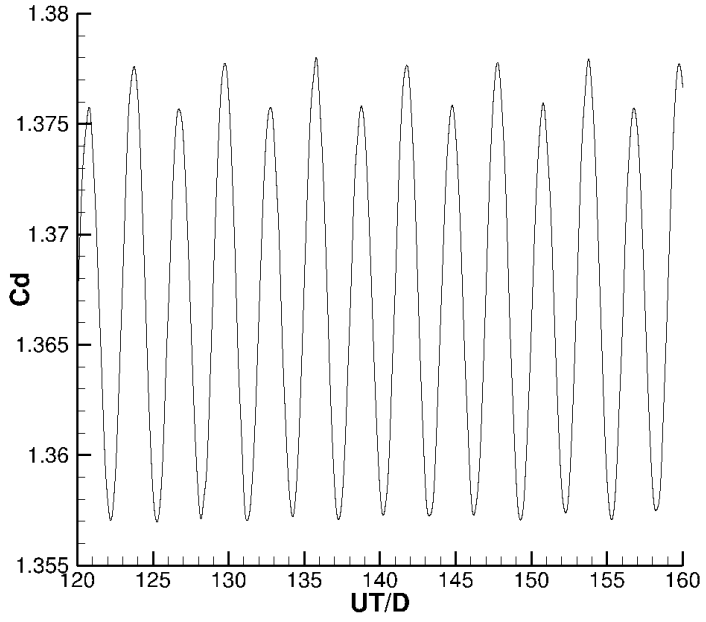

Figure 4.14: Drag coefficient against normalized physical time at Re = 100 by SDRT $_2$.

Table 4.5: SDRT results compared to benchmark solutions for flow over a cylinder at Re = 100.

	Park et al.	Sharman et al.	Current work
Year	1998	2005	-
Blockage ratio	0.01	0.02	0.02
Strouhal number	0.165	0.164	0.166
Cl'	0.23	0.23	0.23
Cl'_v	0.030	0.030	0.030
Cl'_p	0.21	0.20	0.20

Data of Park is obtained from [16].
Data of Sharman is obtained from [19].

Chapter 5: Conclusions and Future Work

In this study, the high-order spectral-difference Raviart-Thomas (SDRT) method is successfully extended to simulate viscous flows using unstructured grids. The stability of SDRT scheme on meshes with quadrilateral elements and mixed elements was analyzed and tested. Since there is no existing stable SDRT schemes for an order of accuracy higher than the fourth-order, we first made several attempts using suggested flux point arrangements in [27] but the outcome was not ideal. Further efforts to achieve stability were made by moving flux points. The numbers of flux points and possible locations were relatively larger than lower-order schemes; this process was computationally expensive. Unfortunately, the efforts were not successful.

The performance of the SDRT method with quadrilateral elements was validated, and more tests were conducted with mixed elements. A new two-dimensional SDRT solver is developed for the compressible Navier-Stokes equations on unstructured grids using triangular-, quadrilateral-, and mixed-element meshes. The results for both inviscid and viscous flow successfully demonstrate high-order accuracy in space.

In the presented study, the SDRT method is stable up to fourth order accuracy, we aim to search for stable SDRT schemes for an order of accuracy that is higher than the fifth-order in the future. Furthermore, the SDRT method is geometrically flexible, and the calculations of the element interface are comparatively simple, it might be appropriate to utilize it in solving fluid–structure interaction problems.

Bibliography

[1] A. Balan, G. May, and J. Schöberl. A stable high-order spectral difference method for hyperbolic conservation laws on triangular elements. *J Comput Phys*, 231(5):2359–2375, 2012.

[2] F. Bassi and S. Rebay. A high-order accurate discontinuous finite element method for the numerical solution of the compressible Navier–Stokes equations. *J Comput Phys*, 131(2):267 – 279, 1997.

[3] P. Castonguay, P. E. Vincent, and A. Jameson. A new class of high-order energy stable flux reconstruction schemes for triangular elements. *J Sci Comput*, 51(1):224–256, 2012.

[4] B. Cockburn and C.W. Shu. TVB Runge-Kutta local projection discontinuous Galerkin finite element method for conservation Laws II: General framework. *Math Comput*, 52(186):411–435, 1989.

[5] J. Flores, J. Barton, T. Holst, and T. Pulliam. Comparison of the full-potential and Euler formulations for computing transonic airfoil flows. In *Ninth international conference on numerical methods in fluid dynamics*, pages 213–218, 1985.

[6] T. Hughes. *The finite element method: linear static and dynamic finite element analysis*. Courier Corporation, 2012.

[7] A. Jameson, W. Schmidt, and E. Turkel. Numerical solution of the Euler equations by finite volume methods using Runge-Kutta time stepping schemes. In *14th fluid and plasma dynamics conference*, page 1259, 1981.

[8] F. Jia, J. Ims, Z. J. Wang, J. Kopriva, and G.M. Laskowski. An evaluation of a commercial and a high order FR/CPR flow solvers for industrial large eddy simulation. In *2018 AIAA aerospace sciences meeting*, page 0827, 2018.

[9] D.A. Kopriva. A staggered-grid multidomain spectral method for the compressible Navier–Stokes equations. *J Comput Phys*, 143(1):125–158, 1998.

[10] C. L. Liang, A. S. Chan, and A. Jameson. A p-multigrid spectral difference method for two-dimensional unsteady incompressible Navier–Stokes equations. *Comput Fluids*, 51(1):127–135, 2011.

[11] C. L. Liang, A. Jameson, and Z. J. Wang. Spectral difference method for compressible flow on unstructured grids with mixed elements. *J Comput Phys*, 228(8):2847–2858, 2009.

[12] C. L. Liang, S. Premasuthan, A. Jameson, and Z. J. Wang. Large eddy simulation of compressible turbulent channel flow with spectral difference method. In *47th AIAA aerospace sciences meeting including the new horizons forum and aerospace exposition*, page 402, 2009.

[13] Y. Liu, M. Vinokur, and Z. J. Wang. Spectral difference method for unstructured grids I: Basic formulation. *J Comput Phys*, 216(2):780–801, 2006.

[14] G. May. On the connection between the spectral difference method and the discontinuous Galerkin method. *Commun Comput Phys*, 9(04):1071–1080, 2011.

[15] G. May and J. Schöberl. Analysis of a spectral difference scheme with flux interpolation on Raviart-Thomas elements. *Aachen Inst. Adv Study Comput Eng Sci*, 1:1–11, 2010.

[16] J. Park, K. Kwon, and H. Choi. Numerical solutions of flow past a circular cylinder at Reynolds numbers up to 160. *KSME Int J*, 12(6):1200–1205, 1998.

[17] W. H. Reed and T. R. Hill. Triangular mesh methods for the neutron transport equation. Technical report, Los Alamos Scientific Lab., N. Mex.(USA), 1973.

[18] V. V Rusanov. Calculation of interaction of non-steady shock waves with obstacles. *Journal of Computational Math Physics USSR*, 1:261–279, 1961.

[19] B. Sharman, F. S. Lien, L. Davidson, and C. Norberg. Numerical predictions of low Reynolds number flows over two tandem circular cylinders. *Int J Numer Methods Fluids*, 47(5):423–447, 2005.

[20] R. J. Spiteri and S. J. Ruuth. A new class of optimal high-order strong-stability-preserving time discretization methods. *SIAM J Numer Anal*, 40(2):469–491, 2002.

[21] Y. Z. Sun, Z. J. Wang, and Y. Liu. High-order multidomain spectral difference method for the Navier-Stokes equations on unstructured hexahedral grids. *Commun Comput Phys*, 2(2):310–333, 2007.

[22] D. J. Tritton. Experiments on the flow past a circular cylinder at low Reynolds numbers. *J Fluid Mech*, 6(04):547–567, 1959.

[23] K. Van den Abeele, C. Lacor, and Z. J. Wang. On the stability and accuracy of the spectral difference method. *J Sci Comput*, 37(2):162–188, 2008.

[24] B. C. Vermeire, F. D. Witherden, and P.E. Vincent. On the utility of gpu accelerated high-order methods for unsteady flow simulations: A comparison with industry-standard tools. *J Comput Phys*, 334:497–521, 2017.

[25] J. f. Wang, C. L. Liang, and M. S. Miesch. A compressible high-order unstructured spectral difference code for stratified convection in rotating spherical shells. *J Comput Phys*, 290:90–111, 2015.

[26] Z. J. Wang, Y. Liu, G. May, and A. Jameson. Spectral difference method for unstructured grids II: Extension to the Euler equations. *J Sci Comput*, 32(1):45–71, 2007.

[27] D. M. Williams, L. Shunn, and A. Jameson. Symmetric quadrature rules for simplexes based on sphere close packed lattice arrangements. *J Comput Appl Math*, 266:18–38, 2014.

[28] L. Xie, M. Xu, B. Zhang, and Z. H. Qiu. A new spectral difference method using hierarchical polynomial bases for hyperbolic conservation laws. *J Comput Phys*, 284:434–461, 2015.

[29] B. Zhang and C. L. Liang. A simple, efficient, and high-order accurate curved sliding-mesh interface approach to spectral difference method on coupled rotating and stationary domains. *J Comput Phys*, 295:147–160, 2015.